1   # An investigation on hygroscopic properties of 15 black carbon

2   # (BC)-containing particles from different carbon sources: Roles

3   # of organic and inorganic components

5   Minli Wang[a], Yiqun Chen[a], Heyun Fu[a], Xiaolei Qu[a], Bengang Li[b], Shu Tao[b], and

6   Dongqiang Zhu[a,b,*]

7   [a] State Key Laboratory of Pollution Control and Resource Reuse, School of the

8   Environment, Nanjing University, Jiangsu 210046, China

9   [b] School of Urban and Environmental Sciences, Key Laboratory of the Ministry of

10   Education for Earth Surface Processes, Peking University, Beijing 100871, China

13   Manuscript prepared for *Atmospheric Chemistry and Physics*

14   [*]Corresponding author. Tel.: +86 010-62766405. E-mail: zhud@pku.edu.cn (D. Zhu)

Abstract

16   The hygroscopic behavior of black carbon (BC)-containing particles (BCPs) has a

17   significant impact on global and regional climate change. However, the mechanism

18   and factors controlling the hygroscopicity of BCPs from different carbon sources are

19   not well understood. Here, we systematically measured the equilibrium and kinetics of

20   water uptake by 15 different BCPs (10 herb-derived BCPs, 2 wood-derived BCPs, and

21   3 soot-type BCPs) using gravimetric water vapor sorption method combined with

22   in-situ diffuse reflectance infrared Fourier transform spectroscopy (DRIFTS). In the

23   gravimetric analysis, the sorption/desorption equilibrium isotherms were measured

24   under continuous-stepwise water vapor pressure conditions, while the kinetics was

25   measured at a variety of humidity levels obtained by different saturated aqueous salt

26   solutions. The equilibrium water uptake of the tested group of BCPs at high relative

27   humidity (> 80%) positively correlated to the dissolved mineral content (0.01–13.0

28   wt%) ($R^2 = 0.86$, $P = 0.0001$), the content of the thermogravimetrically analyzed

29   organic carbon (OC_{TGA}, 4.48–15.25 wt%) ($R^2 = 0.52$, $P = 0.002$), and the content of

30   the alkali-extracted organic carbon (OC_{AE}, 0.14–8.39 wt%) ($R^2 = 0.80$, $P = 0.0001$). In

31   contrast, no positive correlation was obtained with the content of total organic carbon

32   or elemental carbon. Among the major soluble ionic constituents, chloride and

33   ammonium were each correlated with the equilibrium water uptake at high relative

34   humidity. Compared with the herbal BCPs and soot, the woody BCPs had much lower

35   equilibrium water uptake, especially at high relative humidity, likely due to the very

36   low dissolved mineral content and OC content. The DRIFTS analysis provided

37   generally consistent results at low relative humidity. The kinetics of water uptake

38   (measured by pseudo-second-order rate constant) correlated to the content of OC_{TGA}

39   and OC_{AE} as well as the content of chloride and ammonium at low relative humidity

40 (33%), but to the porosity of BCPs at high relative humidity (94%). This was the first

41 study to show that BCPs of different types and sources had greatly varying

42 hygroscopic properties.

43 **1. Introduction**

44 Black carbon (BC) refers to a collective term of refractory and insoluble aggregates of

45 small carbon spherules generated from incomplete combustion of biomass and fossil

46 fuels (Bond et al., 2013). BC-containing particles (BCPs) are ubiquitous in the

47 atmosphere and are a major component of atmospheric carbonaceous aerosols

48 (Schwarz et al., 2008). Due to the strong ability to absorb visible light (Yuan et al.,

49 2015), BCPs cause positive radiative forcing effects on climate and are considered an

50 important factor driving global warming (Matthews et al., 2009). Once immersed into

51 cloud droplets, BCPs can also facilitate water evaporation and cloud dispersion via

52 enhanced absorption of solar radiation, and thus produce indirect radiative forcing

53 effects (Powelson et al., 2014). Additionally, the large specific surface area of BCPs

54 creates a potential for heterogeneous reactions with trace gases (such as volatile

55 halocarbons) in the atmosphere (Qiu et al., 2012), therefore heavily impacting

56 atmospheric chemistry and air quality. Hygroscopicity is a key determinant of

57 physical, chemical, and optical properties of BCPs by changing particle size, phase

58 state, and quality and morphological development, which in turn affect aerosol

59 radiation effect, formation of cloud and ice nuclei, and heterogeneous chemical

60 reactions (Bond et al., 2013; Liu et al., 2018). Furthermore, the hygroscopicity of

61 BCPs is an important factor contributing to the risk of human respiratory infections,

62 cardiovascular diseases, and other infectious diseases (Haddrell et al., 2015).

63 Inherited from parent carbon source or produced from combustion process, large

64 content of inorganic impurities are often present in BCPs, consisting of a variety of

65 amorphous or crystalline salts (sulfates, chlorides, etc.) as well as semi-crystalline

66 minerals (such as silica) (Stanislav et al., 2013). Despite the relatively low content, the

67 inorganic components play in BCPs a significant role in water uptake, depending on

68 their types, contents, and mixing ratios (Lewis et al., 2009). As the factors and

69 processes governing the hygroscopic deliquescence of inorganic salts are very

70 complicated (Reid et al., 2005; Zhang et al., 2012), it is of a great challenge to assess

71 the contribution of a specific salt to the overall hygroscopicity of BCPs, and thus, its

72 role is still controversial. Previous studies suggested that KCl was responsible for the

73 high hygroscopicity of BCPs produced by fresh biomass burning (Posfai et al., 2003),

74 while the presence of K_2SO_4 or KNO_3 caused the low hygroscopicity of BCPs

75 produced by aged biomass burning (Li et al., 2003).

76 The organic components in BCPs consist of graphitized elemental carbon (EC) and

77 non-condensed, amorphous organic carbon (OC) (Lian and Xing, 2017). The

78 contribution of EC to the overall hygroscopicity of BCPs is considered low due to the

79 very high hydrophobicity (Seisel et al., 2005). The role of OC in the hygroscopic

80 growth of BCPs is intricate and debatable. The positive effect of OC is mainly

81 attributed to water absorption by the oxygen-containing functional groups (Fletcher et

82 al., 2007; Suda et al., 2014). The negative effect of OC is suggested to stem from the

83 impeded mass transfer process of water molecules by formation of coatings on

84 hygroscopic minerals or inhomogeneous morphology inside the particle (Sjogren et al.,

85 2007; Stemmler et al., 2008). In addition to the total content, the molecular weight,

86 water solubility, surface tension, and type and content of functional groups of OC

87 were all found to influence the overall hygroscopicity of BCPs. Moreover, the effect

88 of OC on BCPs hygroscopicity is further complicated by the formation of organic

89 minerals (presumably through strong covalent bonds) (Archanjo et al., 2014; Reid et

90   al., 2005; Zuend et al., 2011).

91   The carbon sources for BCPs released into the atmosphere are expected to be highly

92   diversified and cover a wide range of plant biomass, coals, and refined oil products,

93   although their quota can hardly be accurately assessed (Andreae and Gelencser, 2006).

94   The chemical compositional, structural, and morphological properties of BCPs depend

95   significantly on carbon sources and combustion conditions (Xiao et al., 2018). For

96   instance, crop residue-derived biochar often has higher mineral content than

97   wood-derived charcoal, while biochar formed at higher pyrolysis temperatures

98   generally have higher aromaticity, specific surface area, and pore volume but lower

99   polarity than biochar formed at lower temperatures (Wei et al., 2019). Compared with

100   char and charcoal, soot (another type of BCPs) produced from fossil fuel combustion

101   is comprised of more regular shaped, chain-like agglomerates of primary particles,

102   which consist of perturbed graphitic layers oriented concentrically in an onion-like

103   fashion (Nienow and Roberts, 2006). Previous studies on hygroscopicity of BCPs

104   have mainly focused on wood-derived BCPs (Carrico et al., 2010; Day et al., 2006),

105   whereas BCPs from other carbon sources has been largely overlooked. It remains

106   unclear whether BCPs from different carbon sources would differ significantly in

107   hygroscopicity.

108   Herein we systematically investigated the equilibrium and kinetics of water uptake

109   by 15 different BCPs derived from wood, herb, coal, and diesel at varying relative

110   humidity (RH) levels by gravimetric sorption and in-situ diffuse reflectance infrared

111   Fourier transform spectroscopy (DRIFTS). The chemical, compositional, and

112   structural properties of the tested group of BCPs were thoroughly characterized to

113   unveil the key factors controlling the hygroscopic properties.

114   **2. Experimental methods**

2.1. Preparation of BCPs

A total of 15 BCPs were tested, including 10 herb-derived BCPs, 2 wood-derived BCPs, and 3 soot-type BCPs. The herbs used for preparation of herbal BCPs were amaranth, peanuts, pea, grass, rice, wheat, corn, millet, sorghum (Nantong, Jiangsu Province, China), and bamboo (Lishui, Zhejiang Province, China), and the woods used for preparation of woody BCPs were red pine and poplar (Lishui, Zhejiang Province, China). The dried and dehydrated biomass was pulverized into a fine powder using a high-speed pulverizer (FW 100, Tianjin Taisite Instrument, China), and pyrolyzed in a muffle furnace under an oxygen-limited conditions. The oven temperature was programmed to increase from 20 to 400 ℃ in 2 h and maintained at 400 ℃ for 3 h. The Weifu diesel soot was purchased from Wuxi Weifu Automotive Diesel System Co., Ltd. (Jiangsu Province, China). According to the information provided by the manufacturer, the soot was produced under laboratory conditions by burning diesel (Diesel # 5, China) at 1000 ℃ and was collected by a diesel particulate filter (NGK-6000YE) from the exhaust stream at a carbon deposition temperature of 250 ℃. The diesel engine soot was collected in outdoor conditions from the freshly discharged exhaust particles on the tailpipe of a diesel truck (Dongfeng, CY4100, 2015, China) equipped with a diesel engine (CY4100Q, 3.7 L, Diesel # 0) and a diesel particulate filter (BST-5L-QCD). The household soot was collected on the inner wall of a stove chamber (Linkou County, Heilongjiang Province, China) 1 hour later after burning of coal and wood for winter cooking and heating under limited oxygen exposure. The obtained samples of BCPs were further ground to pass a 100-mesh sieve (0.15 mm) and stored sealed in a brown glass bottle at 4 ℃.

2.2. Characterization of BCPs

Elemental analysis (EA) was performed using a Vario micro cube elemental analyzer

140 (Elementar, Hanau, Germany). Surface elemental compositions were measured by

141 X-ray photoelectron spectroscopy (XPS) (PHI 5000 VersaProbe, UlVAC-PHI, Japan).

142 Mineral compositions were measured by X-ray fluorescence (XRF) (ARL-9800, ARL

143 Corporation, Switzerland). Fourier-transform infrared (FTIR) spectra were recorded

144 on a Bruker Tensor 27 Karlsruhe spectrometer (Germany) using KBr pellets in the

145 range of 400 to 4000 cm^{-1}. X-ray diffraction (XRD) spectra were recorded on an AXS

146 D8 Advance spectrometer (Germany) using Cu Kα radiation at a 2θ angle ranging

147 from 5 to 70°. Raman spectra were collected on a Horiba Jobin Yvon LabRam

148 HR-800 spectrometer equipped with a 514 nm laser (France). N_2 adsorption isotherms

149 to the 15 BCPs were obtained on a Micrometrics ASAP 2020 (Micromeritics

150 Instrument Co., Norcross, GA, USA) apparatus at -196 ^{o}C (77 K).

151   Three different methods, thermogravimetric analysis (TGA), alkali extraction, and

152 water extraction, were explored to quantify the content of OC in BCPs (referred to as

153 OC_{TGA}, OC_{AE}, and OC_{WE}, respectively). The content of OC_{TGA} was measured as the

154 weight loss during the heating of BCPs from 30 to 300 ℃ at a ramp of 10 ℃ per

155 minute in a nitrogen flow (Han et al., 2013) using a TGA 8000 analyzer (PerkinElmer,

156 USA). To measure the content of OC_{AE}, the sample of BCPs was mixed with 0.1 M

157 NaOH at a solid-to-solution ratio of 1: 10 (w/w) and magnetically stirred for 12 h,

158 followed by filtration through a 0.45-μm filter membrane (Pall, USA) (Song et al.,

159 2002). The filtrate was collected and acidified (pH 1.0 with 6 M HCl), and the total

160 organic carbon (TOC) content of the sample was measured by a TOC analyzer

161 (TOC-5000A, Shimadzu, Japan). For the three selected BCPs (Grass, Wheat, and

162 Household soot), the precipitates formed by acidification were further separated by

163 centrifugation and dialyzed in deionized (DI) water by dialysis bag (500 Da, Union

164 Carbide, USA) until no chloride ion was detected by $AgNO_3$, and then freeze-dried.

165   The elemental compositions of the three prepared OC_{AE} were measured by EA. To

166   measure the content of OC_{WE} and dissolved minerals, the suspended BCPs in DI

167   water (BCPs-to-water ratio of 1: 10, w/w) was sonicated in a water bath for several

168   minutes, and the mixture was filtered through a 0.45-μm membrane. The

169   suspension/sonication procedure was repeated for 6 times. The filtrate was collected

170   and subjected to TOC analysis to obtain the content of OC_{WE}. The concentrations of

171   ionic constituents (Cl^-, NO_3^-, PO_4^{3-}, SO_4^{2-}, F^-, COO^-, $C_2O_4^{2-}$, Na^+, NH_4^+, K^+, Mg^{2+},

172   Ca^{2+}, Al^{3+})   in   the   filtrate   were   measured   using   a

173   Dionex ICS-1100 ion chromatography (Thermo Scientific, USA). The cations were

174   eluted using 20 mM methanesulfonic acid on a Dionex IonPac CS12A column (4 ×

175   250 mm), while the anions were eluted using an eluent of 4.5 mM Na_2CO_3 and 0.81

176   mM $NaHCO_3$ on a Dionex IonPac AS14A column (4 × 250 mm). The filtrate was

177   further freeze-dried and baked at 600 ℃ for 6 h to remove organic components. The

178   remaining ash was weighed to determine the content of dissolved minerals in BCPs. A

179   portion of the ash was extracted three times using DI water at a solid-to-solution ratio

180   of 1:10 (w/w) under sonication, and the salinity of the extract was measured by a

181   ST3100C conductivity meter (OHAUS, USA). All reagents and chemicals used

182   were of analytical reagent grade.

183   **2.3. Measurement of hygroscopicity of BCPs**

184   The hygroscopicity of BCPs at varying RH was measured by gravimetric method

185   combined with in-situ DRIFTS. The water vapor sorption/desorption isotherms to

186   BCPs under a range of continuous-stepwise water vapor pressures were acquired on

187   a 3H-2000 PW Multi-stations Gravimetric Method Steam Adsorption Instrument

188   (Beijing, China) at 25 ℃ using an approach similar to that in previous studies (Gu et

189   al., 2017). The instrument consists of two main parts: a balance chamber to determine

190 the sample mass to an accuracy ±1 μg and a humidity chamber to regulate the water

191 vapor pressure to the desired value as monitored online by a pressure sensor. Prior to

192 testing, the BCPs (about 10 mg) were dried at 70 ℃ under vacuum for 12 h to remove

193 residual water vapor and set a baseline for comparison of water vapor adsorption

194 behaviors among different samples. The amount of water sorbed to BCPs was

195 monitored as the mass difference before and after sorption. The amount of water

196 sorbed to the sample tube was measured and showed to be negligible ($<$ 0.05% of

197 the amount of water sorbed to BCPs). The water vapor pressures ranging from 10 to

198 94% RH were applied to the sorption isotherm branch in a stepwise increasing

199 sequence and to the desorption isotherm branch in a stepwise decreasing sequence.

200 The kinetics of water sorption to BCPs was measured on a 100 mm closed quartz

201 chamber (Jiangsu Province, China) using a gravimetric method similar to that in

202 previous studies (Yuan et al., 2014). Approximately 100 mg of BCPs was dried at

203 70 ℃ under vacuum for 12 h, weighed in a 10-mL beaker, and placed in a chamber

204 under controlled humidity conditions based on different saturated aqueous salt

205 solutions according to ASTM E104-02 (2007). The saturated solutions of CH_3COOK,

206 $MgCl_2$, K_2CO_3, $LiNO_3$, NaCl, KCl, and KNO_3 provided RH of 23%, 33%, 43%, 47%,

207 75%, 84%, 94%, respectively at 25 ℃. The sample was continuously weighed and

208 recorded over a period of time (48 h for low humidity and 96 h for high humidity) to

209 monitor the amount of sorbed water. The RH was monitored in real time using a

210 Honeywell HIH4000 hygrometer (USA) with measurement variance was less than 5%.

211 Sorption equilibrium was reached in the late stage of the experiment as evidenced by

212 the stabilized constant value of sample mass. In addition to kinetic data, sorption

213 isotherms were also collected for the seven selected RH levels using the measured

214 mass under equilibrium conditions.

215   Samples of BCPs equilibrated at different RH levels were characterized by in situ

216   DRIFTS using a Bruker Tensor 27 spectrometer equipped with a high-sensitivity

217   mercury-cadmium-telluride (MCT) detector working under liquid N_2 conditions and a

218   chamber fitted with ZnSe windows (Harrick Scientific, USA). About 10 mg of BCPs

219   pre-dried at 70 ℃ under vacuum for 12 h was transferred to the chamber which was

220   connected to a gas feeding system. The chamber was sealed and purged with

221   high-purity N_2 at a flow rate of 100 mL per minute for at least 3 h to remove

222   pre-adsorbed gases on BCPs and to minimize the interference of environmental CO_2.

223   The humidity in the chamber was regulated by mixing high-purity N_2 and saturated

224   water vapor at 25 ℃ with varying ratios and monitored in real time by a hygrometer

225   (Vaisala Humitter, Australia). The sample was equilibrated with the gas mixture in the

226   chamber for at least 30 minutes to reach sorption equilibrium based on pre-determined

227   kinetics. The spectra were acquired by co-adding and averaging a plurality of 500

228   scans with a resolution of 4 cm^{-1} (Song and Boily, 2013). The amount of water sorbed

229   to BCPs was monitored by the integrated intensity of the O-H stretching region from

230   2750 to 3660 cm^{-1} (Ghorai et al., 2011).

231   **3. Results and discussion**

232   **3.1. Characteristics of BCPs**

233   Bulk elemental compositions by EA and surface elemental compositions by XPS are

234   summarized in Table S1. The bulk elemental compositions of all BCPs were

235   dominated by C and O, together accounting for 54%–96% of the total. However, the

236   bulk C, O compositions differed significantly among the 15 BCPs, ranging from 32 to

237   76% for C and from 16 to 69% for O. With the exception of the woody BCPs, the

238   differences were apparent within each category of the herbal BCPs and the soot.

239   Similarly, the surfaces of all the 15 BCPs were dominated by C and O; however, the

240   differences of the surface C, O compositions among the 15 BCPs were much smaller

241   compared to the bulk C, O compositions. Besides C and O, EA detected low amounts

242   of N ($<$ 3.7%) and S ($<$ 1.8%), and XPS detected low amounts of N ($<$ 4.3%), Si ($<$

243   5.6%), and S ($<$ 0.6%). The contents of oxygen-containing groups in the 15 BCPs

244   were qualitatively compared by the FTIR spectra (Figure S1). All the tested BCPs

245   except Weifu diesel soot showed characteristic peaks of esters (1700 cm^{-1}), ketones

246   (1613, 1100 cm^{-1}), and phenols (1270 cm^{-1}) (Keiluweit et al., 2010), generally with

247   larger peak intensities observed for herbal BCPs and household soot.

248   Table 1. Chemical, compositional, and pore properties of different BCPs.

BCPs	OC			EC^d	Dissolved minerals	Total Porosity[e]	SSA^f
	$OC_{TGA}{}^a$ (wt%)	$OC_{AE}{}^b$ (wt%)	$OC_{WE}{}^c$ (wt%)	(wt%)	(wt%)	$(m^3\,g^{-1})$	$(m^2\,g^{-1})$
Amaranth	6.24	2.6	1.75	25.84	10.8	0.004	0.314
Grass	7.24	2.37	1.01	51.56	4.8	0.008	5.587
Peanuts	7.45	1.78	0.8	41.86	4.2	0.002	0.192
Pea	9.59	1.98	0.09	54.48	3.6	0.005	4.679
Rice	6.81	0.6	0.11	48.06	0.6	0.023	31.88
Wheat	8.25	1.82	0.37	42.65	5.8	0.01	7.382
Millet	9.41	1.97	0.93	32.25	8	0.023	8.319
Corn	6.55	0.14	0.32	46.47	1.8	0.028	28.6
Sorghum	9.09	1.12	0.62	55.26	4.8	0.001	0.192
Bamboo	6.84	0.23	0.12	61.7	0.6	0.029	51.94
Red pine	7.4	0.2	0.05	62.59	0.01	0.032	64.24
Poplar	7.58	0.19	0.09	64.22	0.6	0.071	107.6
Diesel engine soot	9.57	1.4	0.78	27.37	3.6	0.021	6.119
Weifu diesel soot	4.48	0.57	0.13	71.98	3.4	0.484	194.6
Household soot	15.25	8.39	2.24	21.83	13	0.012	7.79

249   [a]Content of organic carbon determined by TGA. [b]Content of alkali-extractedorganic

250   carbondetermined by TOC analysis. [c]Content of water-extracted organic

251   carbondetermined by TOC analysis. [d]Determined by subtracting OC_{TGA} content from

252   total organic carbon content by EA. [e]Total pore volume determined by N_2 adsorption

253   at 0.97 atmosphere pressure. [f]Specific surface area determined by the BET method.

254   Table 1 summarizes the contents of OC (OC_{TGA}, OC_{AE}, and OC_{WE}) of the 15 BCPs

255   by TGA, alkali extraction, and water extraction, respectively. For a given BCPs, the

256   contents of the three types of OC differed pronouncedly, with an increasing order of

257    $OC_{WE} < OC_{AE} < OC_{TGA}$. The OC content also differed within the tested group of

258   BCPs, ranging from 0.05 to 2.24wt% for OC_{WE}, from 0.14 to 8.39wt% for OC_{AE}, and

259   from 4.48 to 15.25wt% for OC_{TGA}. Compared with the EC (graphitized carbon), the

260   three types of OC are non-condensed, amorphous, and more rich in oxygen-containing

261   functional groups, which was evidenced by the fact that the OC_{AE} from the three

262   selected BCPs (Grass, Wheat, and Household soot) had markedly higher bulk

263   compositions of O (results presented in Table S2). The EC content in BCPs was

264   roughly assessed by subtracting the OC_{TGA} content from the total organic carbon

265   content measured by EA (results presented in Table 1). The calculated EC content

266   negatively correlated with the OC_{AE} content ($R^2 = 0.43$, $P = 0.0079$) for the examined

267   group of BCPs. This relationship was reasonable as EC was comprised of mature,

268   thermodynamically stable graphitized carbons, while OC was comprised of the less

269   mature and less aromatic constituents remaining after pyrolysis. Except for Weifu

270   diesel soot, the two woody BCPs had the highest EC, but the lowest OC_{AE} and OC_{WE}

271   among the 15 BCPs.

272   The relative abundance of EC in BCPs was also assessed by Raman spectroscopy

273   (Figure S2). The spectra of all the tested BCPs were dominated by a D band at 1340

274   cm^{-1} and a G band at 1580 cm^{-1}, which were ascribed to carbon network defects and

275   the E_{2g} mode of the graphitized carbon, respectively (Pimenta et al., 2007). Thus, the

276   ratio of these two bands (I_D/I_G) was inversely proportional to the in-plane crystallite

277   size of graphitized carbons of BCPs (Cancado et al., 2006). The I_D/I_G ratio of the

278   woody BCPs (0.51–0.59) was less than those of the herbal BCPs (0.88–1.09) and the

279   soot (0.77–1.12) (Table S3), suggesting larger sizes of graphitized carbons in the

280   woody BCPs, which was consistent with the results of OC compositions.

281   The contents of dissolved minerals of the 15 BCPs are listed in Table 1, and their

282   salinities in water extracts are listed in Table S5. The two woody BCPs had the lowest

283   contents of dissolved minerals and salinities, while these contents in herbal BCPs and

284   soot were higher and varied greatly. The mineral compositions characterized by XRF

285   are listed in Table S6. Si-, K-rich minerals were the two major inorganic constituents

286   in the herbal BCPs and woody BCPs. Moreover, these two types of BCPs generally

287   contained trace amounts of S-, Cl-, Ca-, P-, Mg-, Na-, Fe-, and Al-minerals, with

288   lower contents observed for the woody BCPs. The three soot had very different

289   mineral compositions. Household soot was dominated by S-, Ca-, Si-, and Cl-minerals,

290   Diesel engine soot was dominated by S-, Ca-, and Fe-minerals, while Weifu diesel

291   soot contained negligible mineral compositions. As reflected by the observed

292   characteristic peaks and associated peak intensities in the XRD spectra (Figure S3),

293   the herbal BCPs and Household soot contained more mineral species with higher

294   contents than other BCPs, whereas the two woody BCPs and Weifu diesel soot

295   contained the least species and contents of minerals. Potassium salts, amorphous silica,

296   and sulfates were the major minerals in the herbal BCPs. Soot had the largest content

297   of sulfates among the tested BCPs. According to the ion chromatograph analysis

298   (results presented in Figure S4 and Table S7), the major water-extracted cationic

299   species from the tested BCPs were NH_4^+, K^+, and Ca^{2+}, and the major anionic species

300   were SO_4^{2-}, Cl^-, and $C_2O_4^{2-}$. The herbal BCPs had high contents of K^+, $C_2O_4^{2-}$, and Cl^-,

301   while the soot had high content of SO_4^{2-}.

302   The Brunauer–Emmett–Teller (BET) specific surface area and total porosity

303   measured by N_2 adsorption are also summarized in Table 1. A huge disparity of

304   specific surface area was shown among the 15 BCPs and among the BCPs within each

305   category, ranging from 6 to 200 m^2 g^{-1} for the soot, from 60 to 110 m^2 g^{-1} for the

306   woody BCPs, and from 0.1 to 52 m^2 g^{-1} for the herbal BCPs. The micro- and

307   mesoporosity of the 15 tested BCPs are summarized in Table S4. The herbal BCPs

308   and woody BCPs were dominated by micropores (pore size < 2 nm), which accounted

309   for more than 50% of the total pore volume. Alternatively, mesopores (50 nm > pore

310   size > 2 nm) were the main pore structure of the soot, accounting for more than 61%

311   of the total pore volume.

312   **3.2. Hygroscopic properties of BCPs**

313   **Equilibrium water uptake**. Figure 1 displays sorption and desorption isotherms of

314   water vapor with BCPs plotted as equilibrium water uptake (mg g^{-1}) by unit mass of

315   BCPs under continuous-stepwise water vapor pressure conditions. Figure S5 displays

316   the equilibrium sorption isotherms at selected humidity levels obtained by using

317   saturated aqueous salt solutions. Under similar humidity conditions (80% and 84%),

318   the water uptake by the 15 BCPs was very close between these two humidity

319   regulation methods (Figure S6), reflecting their technical validity. The woody BCPs

320   showed very different sorption isotherm patterns from the herbal BCPs and soot. First,

321   the water sorbing ability of the woody BCPs was much lower. The maximum water

322   uptake observed at the highest RH (94%) was approximately 65 mg g^{-1} by the woody

323   BCPs, but was more than 400 mg g^{-1} for the strongest sorbing herbal BCPs and soot.

324   Second, much larger water-uptake disparities were observed within the group of

325   herbal BCPs and the soot group than within the group of woody BCPs. Additionally,

326   over the examined RH range (10–94%), the water uptake by the woody BCPs

327   increased slowly and linearly with the RH; however, for the herbal BCPs and soot, the

328   water uptake increased more rapidly with the RH, especially under high humidity

329   conditions (RH > 70%).

330
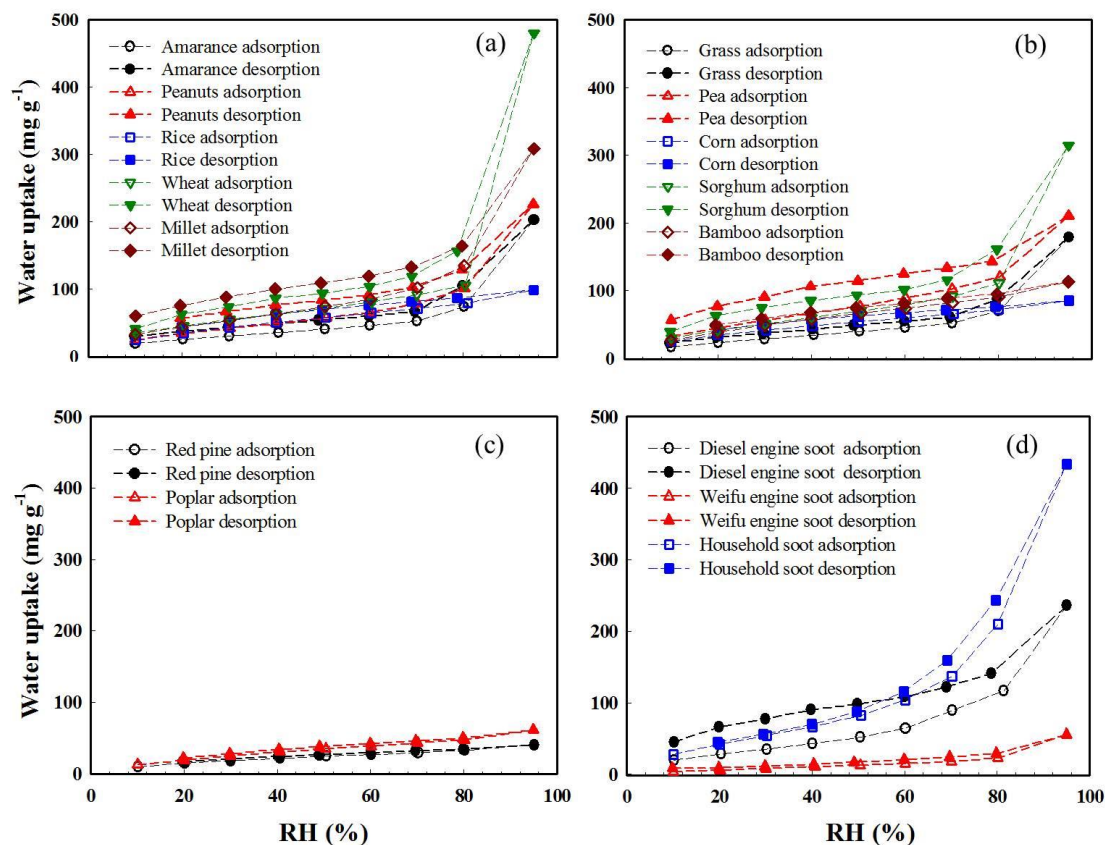
331 Figure 1. Sorption and desorption isotherms of water vapor plotted as water uptake

332 (mg g^{-1}) vs. relative humidity (RH, %) at equilibrium for different BCPs. (a)

333 Subgroup 1 of herbal BCPs. (b) Subgroup 2 of herbal BCPs. (c) Woody BCPs. (d)

334 Soot. Data were collected with single-point.

335 To better understand the underlying mechanisms and factors controlling the

336 hygroscopic properties of BCPs, linear relationships were built between the

337 equilibrium water uptake and a wide variety of compositional and pore property

338 parameters of the whole group of BCPs. Figure 2 displays regression relationships

339 with contents of OC_{TGA}, OC_{AE}, EC, dissolved minerals, major ionic species (NH_4^+, Cl^-,

340 SO_4^{2-}, and $C_2O_4^{2-}$), and total porosity, respectively at 94% RH. The regression

341 relationships at 23% RH were presented in Figure S7. The regression accuracy (R^2

342 and P) values at the 7 different RH levels (23, 33, 43, 47, 75, 84, 94%) are

343 summarized in Table S8. Good positive correlations existed between the water uptake

344 and the contents of OC_{TGA}, OC_{AE}, and dissolved minerals under high humidity

345 conditions (Figure 2a-d). The highest regression accuracy values obtained were $R^2 =$

346 0.82, $P <$ 0.0001 for OC_{TGA} at 84% RH, $R^2 = 0.80$, $P = 0.001$ for OC_{AE} at 94% RH,

347 and $R^2 = 0.86$, $P = 0.0001$ for dissolved minerals at 94% RH. However, the

348 correlations with these constituents became much weaker under low humidity

349 conditions ($R^2 = 0.10–0.32$, $P = 0.247–0.028$ at RH = 23%). It can be concluded that

350 the hygroscopicity of herbal BCPs and soot under high humidity conditions was

351 mainly controlled by the contents of OC and dissolved minerals. On the other hand,

352 the low water sorbing ability of the woody BCPs was due to the very low contents of

353 these constituents. As indicated by the elemental analysis results (Table S2), the OC

354 constituents in the three representative BCPs (Grass, Red pine, and Household soot)

355 contained large amounts of oxygen-containing groups, which expectedly had very

356 high hygroscopicity (Xiao et al., 2013). The very strong water retention ability of

357 dissolved minerals in BCPs was understandable due to the strong hydration of mineral

358 surfaces and ionic constituents. No correlation was observed between the water

359 uptake of BCPs and the total organic carbon content within the whole examined RH

360 range. Notably, a negative correlation was observed with the EC content (Figure 2c),

361 especially under high humidity conditions ($R^2 = 0.54$, $P = 0.0019$ at 94% RH).

362 Compared with the OC in BCPs, the EC was comprised mainly of hydrophobic fuse

363 aromatic hydrocarbons and had much lower amounts of oxygen-containing groups,

364 resulting in the very low water sorbing ability.

365 The above one-factor linear correlation analysis indicted that at high RH the

366 hygroscopicity of BCPs was dominated by OC and dissolved minerals. Consistently, a

367 better positive correlation ($R^2 = 0.90$, $P <$0.0001) could be obtained between the

368 equilibrium water uptake and the contents of OC_{TGA} and dissolved mineral by binary

369 linear regression for the tested group of BCPs (Figure S8). Interestingly, the

370 correlation relationship became poorer as the RH level gradually decreased, and the

371 worst correlation was shown at 23% RH ($R^2 = 0.21$, $P = 0.028$). The results suggested

372 that the hygroscopicity of BCPs at low RH was controlled by different factors.

373

374 Figure 2. Relationships between equilibrium water uptake (mg g^{-1}) vs. compositional

375 and pore property parameters for the group of BCPs at 94% relative humidity. (a)

376 TGA-measured organic carbon (OC$_{TGA}$). (b) Alkali-extracted organic carbon (OC$_{AE}$).

377 (c) Elemental carbon (EC). (d) Dissolved minerals. (e) Ammonium (NH$_4^+$). (f)

378 Chloride (Cl$^-$). (g) Oxalate (C$_2$O$_4^{2-}$). (h) Sulfate (SO$_4^{2-}$). (i) Total porosity.

379 At 94% RH, relatively good positive correlations were observed with NH$_4^+$ and Cl$^-$

380 ($R^2 = 0.50$–0.70, $P = 0.0001$–0.0034), but not with SO$_4^{2-}$ ($R^2 = 0.24$, $P = 0.06$) or

381 C$_2$O$_4^{2-}$ ($R^2 = 0.002$, $P = 0.89$) (Figure 2e-h). No correlation ($R^2 = 0.08$, $P = 0.30$) was

382 observed with the total porosity of BCPs at 94% RH (Figure 2i). Consistently,

383 previous studies reported that chloride salts in biomass burning aerosols had high

384 hygroscopicity (Jing et al., 2017; Posfai et al., 2003). The poor correlation observed

385 for SO_4^{2-} was ascribed to the low hygroscopicity of $CaSO_4$ and K_2SO_4, as evidenced

386 by their very high deliquescent relative humidity (96–97%) (Freney et al., 2007;

387 Preturlan et al., 2019). It is noteworthy that the content of SO_4^{2-} positively correlated

388 with the contents of Ca^{2+} ($R^2 = 0.74$, $P < 0.0001$) and K^+ ($R^2 = 0.69$, $P = 0.0008$) for

389 the tested BCPs. On the other hand, the poor correlation observed for $C_2O_4^{2-}$ was

390 likely due to the formation of less water-soluble compounds (e.g., CaC_2O_4 and

391 $H_2C_2O_4$) that might depress the hygroscopicity (Buchholz and Mentel, 2008).

392 The positive correlations observed with NH_4^+ and Cl^- at 94% RH disappeared at

393 23% RH. Alternatively, a relative good negative correlation ($R^2 = 0.42$, $P = 0.0095$)

394 with the total porosity was shown at 23% RH (Figure S7i). Similarly, a weak negative

395 correlation ($R^2 = 0.21$, $P = 0.083$) was shown with the EC content at 23% RH. The

396 consistency between the total porosity and the EC content was likely due to the

397 dominant role of graphitized carbons (EC) in forming rigid pore structures of BCPs

398 (Han et al., 2014). On the contrary, a weak positive correlation ($R^2 = 0.32$, $P = 0.028$)

399 was observed between the water uptake and the OC_{TGA} content at 23% RH, indicating

400 that the OC constituents were an important factor contributing to the overall water

401 uptake by BCPs under low humidity conditions.

402 As can be seen from the sorption-desorption isotherms in Figure 1, some herbal

403 BCPs (Amarance, Peanuts, Wheat, Millet, Pea, and Sorghum) and soot (Diesel engine

404 soot and Household soot) showed strong hysteresis effect (irreversible sorption),

405 whereas none of the woody BCPs showed hysteresis effect. Irreversible sorption

406 would lower the release of sorbed water molecules from BCPs in the atmosphere

407 when the RH changes from a high level to a low level. The observed hysteresis effect

408 of herbal BCPs and soot likely stemmed from their relatively high contents of OC

409 and/or dissolved minerals (such as Wheat and Household soot). Sorbing water

410 molecules could cause strong and irreversible hydration of organic acids (Petters et al.,

411 2017) and dissolution or phase change of minerals (Adapa et al., 2018), consequently

412 leading to hysteresis effect due to non-identical structures of BCPs between the

413 sorption and desorption branches even at the same RH. The negligible hysteresis

414 effect observed on the two woody BCPs could be attributed to their very low contents

415 of OC and dissolved minerals.

416 The equilibrium water uptake by BCPs was further investigated by DRIFTS. The

417 spectra of representative BCPs (Grass, Red pine, and Household soot) at varying RH

418 are presented in Figure 3a-c. Figure 3d compares the water uptake at 23% RH

419 monitored by the integrated intensity of the O-H stretching region from 2750 to 3660

420 cm^{-1} (Ghorai et al., 2011), along with the water uptake measured by the

421 multi-station gravimetric method for 8 selected BCPs. The identified bands of sorbed

422 water molecules included a combination mode of symmetric stretch around 3423 cm^{-1}

423 and asymmetric stretch stretch around 3253 cm^{-1} (Gustafsson et al., 2005). The broad

424 feature peak centered at 2100 cm^{-1} was assigned to a combined band of bending,

425 libration, and hindered translation modes of water, while the peak centered at 1640

426 cm^{-1} was attributed to the bending mode of water (Ma et al., 2010). The intensities of

427 these peaks/bands increased with increasing RH. As assessed by the integrated

428 intensity of the O-H stretching region (see insets in Figure 3a-c), the water uptake by

429 Grass and Household soot increased gradually with RH from 12 to 80%; however, the

430 water uptake by Red pine rapidly reached saturation at about 28% RH, and kept

431 constant when the RH was further increased. With the exception of Weifu diesel soot,

432 the disparity pattern of water uptake by the 8 selected BCPs at 23% RH monitored by

433 DRIFTS was similar to that monitored by the multi-station gravimetric method

434 (Figure 3d). However, the disparities were very large between these two methods at

435 80% RH (Figure S9), which was probably because the saturated effect encountered in

436 detection of sorbed water molecules by FTIR (Gustafsson et al., 2005) became worse

437 under high humidity conditions. Moreover, the DRIFTS signals of sorbed water

438 molecules might be influenced by the distribution of sorption sites (e.g., minerals vs.

439 OC and exterior vs. interior), and the caused effects might lead to larger deviations

440 under high humidity conditions.

441
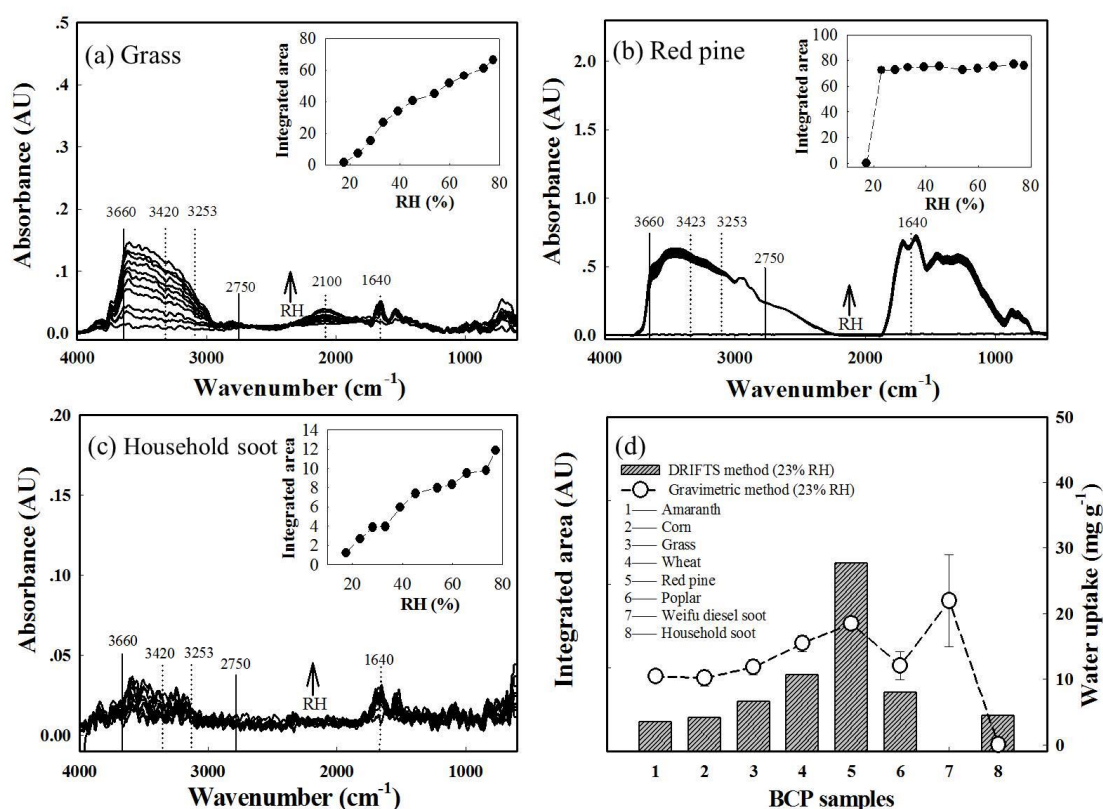
442 Figure 3. Diffuse reflectance infrared Fourier transform spectroscopy (DRIFTS)

443 characterization of equilibrium water uptake by BCPs. (a-c) Spectra for the three

444 representative BCPs (Grass, Red pine, and Household soot) equilibrated at varying

445 relative humidity (RH) levels. (d) Comparison of equilibrium water uptake measured

446 as integrated area of O-H stretching region (2750–3660 cm^{-1}) between 8 selected

447   BCPs at 23% relative humidity. Error bars represent standard variations from

448   duplicate samples. Insets in subfigures (a-c) present water uptake measured as

449   integrated area of O-H stretching region against RH.

450   **Kinetic water uptake.** Figure 4 displays the water vapor sorption kinetics to the 15

451   BCPs at 94% RH obtained by saturated aqueous salt solutions. The sorption kinetics

452   at 33% RH was presented in Figure S10. The two woody BCPs exhibited similar

453   kinetics curves; however, the herbal BCPs and soot showed very different kinetic

454   patterns within each group. The kinetic data were fitted to the pseudo-first-order and

455   pseudo-second-order models, $dq_t/dt = k_1 (q_e\text{-}q_t)$ and $dq_t/dt = k_2 (q_e\text{-}q_t)^2$, respectively,

456   where q_t was the sorbed concentration at time t, q_e was the equilibrium sorbed

457   concentration, and k_1 and k_2 were the pseudo-first-order and pseudo-second-order rate

458   constants, respectively. Note that these two kinetic models were applied only for

459   quantitative comparison of apparent sorption kinetics among different BCPs, but not

460   for illustration of sorption mechanisms. The fitting parameters (q_e k_1, k_2) for the three

461   selected RH levels (33, 47, and 94%) are summarized in Tables S9-S10. The

462   pseudo-second-order model ($R^2 > 0.97$) fits the data better than the pseudo-first-order

463   model ($R^2 = 0.80$–0.99). The calculated k_2 differed greatly among the BCPs within the

464   group of herbal BCPs and the soot group, but was very close between the two woody

465   BCPs. For a given BCPs, the k_2 at a lower RH level was significantly larger than that

466   at a higher RH level. Similar results were reported in previous studies on sorption

467   kinetics of water vapor to activated carbon (Ohba and Kaneko, 2011; Ribeiro et al.,

468   2008). Under low humidity conditions, sorption of water vapor mainly occurs at the

469   active, high-energy binding sites, and the sorption kinetics is fast; alternatively, under

470   high humidity conditions, sorption is governed by the slow pore-filling/condensation

471   process of water molecules within the pores of activated carbon via formation of

472 water clusters around the water molecules already sorbed at the active sites (Nguyen

473 and Bhatia, 2011; Rosas et al., 2008). Due to the small molecular size (0.0958 ×0.151

474 nm, ChemDraw 3D), water molecules could well penetrate into the micropores of

475 BCPs and form water clusters via intermolecular hydrogen bonding. The sorbing

476 ability order of the different types of BCPs varied depending on the examined RH. At

477 33% RH, the k_2 roughly followed a decreasing order of soot (0.5–5.25 $\times$ 10^{-5} g

478 $mg^{-1}s^{-1}$) > woody BCPs (1.57–1.90 $\times 10^{-5}$ g $mg^{-1}s^{-1}$) > herbal BCPs (0.34–2.07 $\times10^{-5}$

479 g $mg^{-1}s^{-1}$); however, no clear trend was shown for high humidity conditions (e.g., RH

480 = 94%), mainly resulting from the larger variances within the group of herbal BCPs

481 and soot group.

482
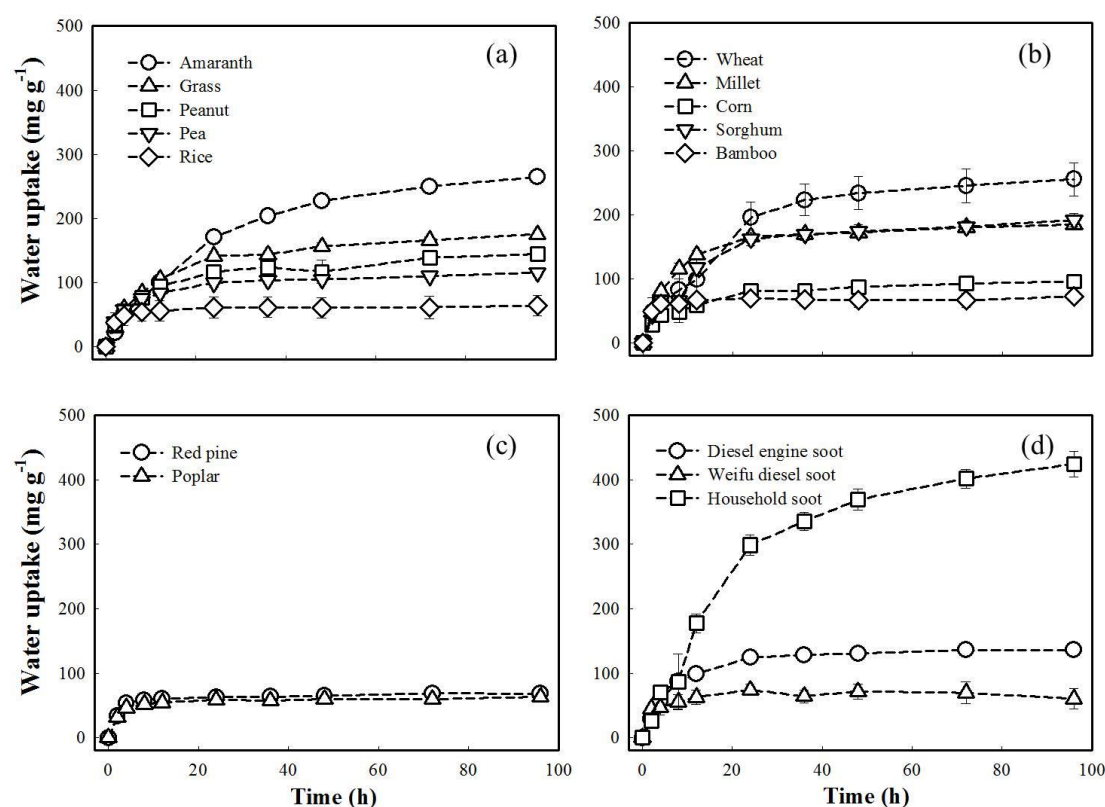
483 Figure 4. Sorption kinetics of water vapor plotted as water uptake (mg g^{-1}) vs. time (h)

484 at 94% relative humidity. (a) Subgroup 1 of herbal BCPs. (b) Subgroup 2 of herbal

485 BCPs. (c) Woody BCPs. (d) Soot. Error bars represent standard variations from

486   duplicate samples.

487   Like for the equilibrium water uptake, the relationships were built between the k_2

488   and the contents of OC_{TGA}, OC_{AE}, EC, dissolved minerals, major ionic species (NH_4^+,

489   Cl^-, $C_2O_4^{2-}$ and SO_4^{2-}), and total porosity, respectively at 94% RH (Figure 5). The

490   regression relationships at 33% RH were presented in Figure S11. The regression

491   accuracy (R^2 and P) values at 33%, 47%, and 94% RH are summarized in Table S11.

492   At 94% RH, a strong positive correlation was observed between the k_2 and the total

493   porosity ($R^2 = 0.82$, $P < 0.0001$), likely resulting from the pore-filling/condensation

494   mechanism. A similar mechanism has been previously proposed to account for the

495   positive correlation observed between the water vapor sorption kinetics and the

496   porosity of activated carbon under high humidity conditions (Nakamura et al., 2010;

497   Velasco et al., 2016). Likewise, a positive correlation ($R^2 = 0.45$, $P = 0.0061$) was

498   observed between the k_2 and the EC content, which could be ascribed to the formation

499   of rigid pore structures dominantly by graphitized carbons (EC) (Han et al., 2014).

500   The correlation between k_2 and total porosity observed at 94% RH disappeared under

501   low and medium humidity conditions. At 33% RH, relatively good positive

502   correlations were observed with the contents of OC_{TGA} ($R^2 = 0.47$, $P = 0.0046$), OC_{AE}

503   ($R^2 = 0.44$, $P = 0.007$), NH_4^+ ($R^2 = 0.77$, $P < 0.0001$), and Cl^- ($R^2 = 0.60$, $P =$

504   0.0007), but not with $SO4^{2-}$ ($R^2 = 0.11$, $P = 0.2286$) or dissolved minerals ($R^2 = 0.08$,

505    $P = 0.31$). The positive correlations with these constituents were not shown under

506   medium and high humidity conditions. Thus, the constituents of OC and NH_4^+- and

507   Cl^--salts likely provided the primary high affinity, active sites for sorption of water

508   vapor under low humidity conditions.

509
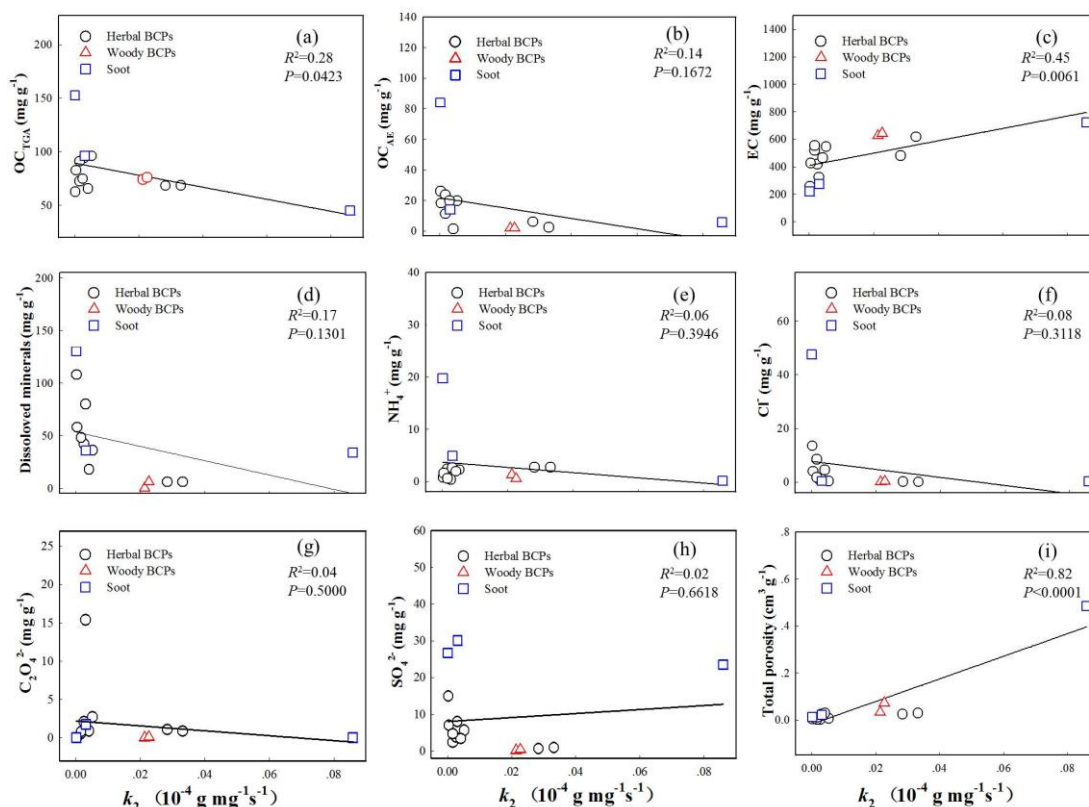
Figure 5. Relationships between pseudo-second water uptake rate constant (k_2) (g mg^{-1}s^{-1}) vs. compositional and pore property parameters for the group of BCPs at 94% relative humidity. (a) TGA-measured organic carbon (OC$_{TGA}$). (b) Alkali-extracted organic carbon (OC$_{AE}$). (c) Elemental carbon (EC). (d) Dissolved minerals. (e) Ammonium (NH$_4^+$). (f) Chloride (Cl$^-$). (g) Oxalate (C$_2$O$_4^{2-}$). (h) Sulfate (SO$_4^{2-}$). (i) Total porosity.

4. Conclusion

The hygroscopic properties of 15 different BCPs (herbal, woody, and soot) were systematically investigated using gravimetric method and DRIFTS. The mechanisms and factors controlling the equilibrium and kinetic water uptake differed among the types of BCPs and depended heavily on the humidity conditions. Linear correlation analyses indicated that the equilibrium water uptake by the tested group of BCPs positively correlated to the contents of OC (OC$_{TGA}$ and OC$_{AE}$), dissolved minerals,

523 and NH_4^+- and Cl^--salts under high humidity conditions, and weakly to the contents of

524 OC only under low humidity conditions. By contrast, negative correlations were

525 observed between the equilibrium water uptake and the EC content. The low water

526 uptake by the woody BCPs could be attributed to the very low contents of OC and

527 dissolved minerals. Thus, the equilibrium water uptake by BCPs was mainly

528 controlled by the hygroscopic constituents of OC and dissolved minerals/salts. The

529 kinetic water uptake by the BCPs could be well described by the pseudo-second-order

530 kinetic model. The calculated rate constant (k_2) positively correlated to the contents

531 OC_{TGA}, OC_{AE}, and NH_4^+- and Cl^--salts under low humidity conditions, and to the total

532 porosity only under high humidity conditions. The fast water uptake kinetics under

533 low humidity conditions was attributed to the binding to high affinity, active sites (OC

534 and salts), which could sorb water vapor fast but had limited contents. Alternatively,

535 the slow water uptake kinetics under high humidity conditions was attributed to

536 pore-filling/condensation of water molecules within the micro- and mesopores of

537 BCPs. This study highlights that the hygroscopic properties of BCPs rely on

538 compositional and structural properties of BCPs as well as humidity conditions.

539 **Author contributions.** DZ provided the original idea and prepared the paper with

540 contributions from all co-authors. MW and YC designed and conducted the research,

541 HF, XQ were involved in the development of the analysis methods. BL, ST reviewed

542 the written document.

543 **Competing interests.** The authors declare that they have no conflict of interest.

544 **Acknowledgments.** This work was supported by the National Natural Science

545 Foundation of China (Grants 21777002, 21920102002, and 41991331).

546 **Appendix A.**

547   Detailed characterization results of the different BCPs can be found in Tables

548   S1-S7. Table S8 lists accuracy (R^2 and P) values for regression on equilibrium water

549   uptake against different variables. Tables S9-S10 present pseudo-first/second-order

550   kinetic model fitting parameters. Table S11 lists accuracy (R^2 and P) values for

551   regression on k_2 against different variables. Figure S1-S4 displays spectroscopic

552   characterization of different BCPs. Figure S5 displays sorption isotherms at selected

553   humidity obtained by using saturated aqueous salt solutions. Figure S6 compares

554   equilibrium water uptake measured by the two different gravimetric methods. Figure

555   S7 displays relationships between equilibrium water uptake and different variables at

556   23% RH. Figure S8 displays the relationship between measured values of equilibrium

557   water uptake at 94% relative humidity vs. predicted values obtained by binary factor

558   regression based on contents of OC_{TGA} and dissolved minerals for the group of BCPs.

559   Figure S9 compares equilibrium water uptake measured by DRIFTS and gravimetric

560   method at high RH. Figure S10 displays sorption kinetics of water uptake at 33% RH.

561   Figure S11 displays relationships between k_2 and different variables at 33% RH.

562

References

Adapa, S., Swamy, D. R., Kancharla, S., Pradhan, S., and Malani, A.: Role of mono- and divalent surface cations on the structure and adsorption behavior of water on mica surface, Langmuir, 34 (48), 2018.

Andreae, M. O., and Gelencser, A.: Black carbon or brown carbon? The nature of light-absorbing carbonaceous aerosols, Atmos. Chem. Phys., 6, 3131–3148, 2006.

Archanjo, B. S., Araujo, J. R., Silva, A. M., Capaz, R. B., Falcao, N. P. S., Jorio, A., and Achete, C. A.: Chemical analysis and molecular models for calcium-oxygen-carbon interactions in black carbon found in fertile Amazonian anthrosoils, Environ. Sci. Technol., 48, 7445–7452, 2014.

Bond, T. C., Doherty, S. J., Fahey, D. W., Forster, P. M., Berntsen, T., DeAngelo, B. J., Flanner, M. G., Ghan, S., Kärcher, B., Koch, D., Kinne, S., Kondo, Y., Quinn, P. K., Sarofim, M. C., Schultz, M. G., Schulz, M., Venkataraman, C., Zhang, H., Zhang, S., Bellouin, N., Guttikunda, S. K., Hopke, P. K., Jacobson, M. Z., Kaiser, J. W., Klimont, Z., Lohmann, U., Schwarz, J. P., Shindell, D., Storelvmo, T., Warren, S. G., and Zender, C. S.: Bounding the role of black carbon in the climate system: A scientific assessment, J. Geophys. Res. Atmos., 118, 5380–5552, 2013.

Buchholz, A., and Mentel, T. F.: Hygroscopic growth of oxalic acid and its ammonium, sodium and potassium salts, Geophys. Res. Abs., 10, EGU2008-A-03795.

Cancado, L. G., Takai, K., Enoki, T., Endo, M., Kim, Y. A., and Mizusaki, H.: General equation for the determination of the crystallite size L-a of nanographite by Raman spectroscopy, Appl. Phys. Lett., 88 (16), 2006.

Carrico, C. M., Petters, M. D., Kreidenweis, S. M., Sullivan, A. P., McMeeking, G. R., Levin, E. J. T., Engling, G., Malm, W. C., and Collett Jr. J. L.: Water uptake and chemical composition of fresh aerosols generated in open burning of biomass,

Atmos. Chem. Phys., 10, 5165–5178, 2010.

Day, D. E., Hand, J. L., Carrico, C. M., Engling, G., and Malm, W. C.: Humidification factors from laboratory studies of fresh smoke from biomass fuels, J. Geophys. Res., 111, D22202, 2006.

Fletcher, A. J., Uygur, Y., and Mark Thomas, K.: Role of surface functional groups in the adsorption kinetics of water vapor on microporous activated carbons, J. Phys. Chem. C., 111, 8349–8359, 2007.

Freney, E. J., Martin, S. T., and Buseck, P. R.: Deliquescence measurements of potassium salts, American Geophysical Union, Fall Meeting, 2007.

Ghorai, S., Laskin, A., and Tivanski, A. V.: Spectroscopic evidence of keto-enol tautomerism in deliquesced malonic acid particles, J. Phys. Chem. A., 115, 4373–4380, 2011.

Gu, W., Li, Y., Zhu, J., Jia, X., Lin, Q., Zhang, G., Ding, X., Song, W., Bi, X., Wang, X., and Tang, M.: Investigation of water adsorption and hygroscopicity of atmospherically relevant particles using a commercial vapor sorption analyzer, Atmos. Meas. Tech., 10, 3821–3832, 2017.

Gustafsson, R. J., Orlov, A., Badger, C. L., Griffiths, P. T., Cox, R. A., and Lambert, R. M.: A comprehensive evaluation of water uptake on atmospherically relevant mineral surfaces: DRIFT spectroscopy, thermogravimetric analysis and aerosol growth measurements, Atmos. Chem. Phys., 5, 3415–3421, 2005.

Haddrell, A. E., Davies, J. F., and Reid, J. P.: Dynamics of particle size on inhalation of environmental aerosol and impact on deposition fraction, Environ. Sci. Technol., 49, 14512–14521, 2015.

Han, C., Liu, Y., and He, H.: Role of organic carbon in heterogeneous reaction of NO_2 with soot, Environ. Sci. Technol., 47, 3174–3181, 2013.

613 Han, L. F., Sun, K., Jin, J., Wei, X., Xia, X. H., Wu, F. C., Gao, B., and Xing, B. S.:

614 Role of structure and microporosity in phenanthrene sorption by natural and

615 engineered organic matter, Environ. Sci. Technol., 48, 11227−11234, 2014.

616 Jing, B., Peng, C., Wang, Y., Liu, Q., Tong, S., Zhang, Y., and Ge, M.: Hygroscopic

617 properties of potassium chloride and its internal mixtures with organic compounds

618 relevant to biomass burning aerosol particles, Sci. Rep., 2, 43573, 2017.

619 Keiluweit, M., Nico, P. S., Johnson, M. G, Kleber, M.: Dynamic molecular structure

620 of plant biomass-derived black carbon (biochar), Environ. Sci. Technol., 44 (4),

621 1247−1253, 2010.

622 Lewis, K. A., Arnott, W. P., Moosmuller, H., Chakrabarty, R. K., Carrico, C. M. ,

623 Kreidenweis, S. M., Day, D. E., Malm, W. C., Laskin, A., Jimenez, J. L., Ulbrich, I.

624 M., Huffman, J. A., Onasch, T. B., Trimborn, A., Liu, L., and Mishchenko, M. I.:

625 Reduction in biomass burning aerosol light absorption upon humidification: roles

626 of inorganically-induced hygroscopicity, particle collapse, and photoacoustic heat

627 and mass transfer, Atmos. Chem. Phys., 9, 8949–8966, 2009.

628 Li, J., Posfai, M., Hobbs, P. V., and Buseck, P. R.: Individual aerosol particles from

629 biomass burning in southern Africa: 2. Compositions and aging of inorganic

630 particles, J. Geophys. Res., 108, 8484, 2003.

631 Lian, F., and Xing, B.: Black carbon (biochar) in water/soil environments: Molecular

632 structure, sorption, stability, and potential risk, Environ. Sci. Technol., 51,

633 13517–13532, 2017.

634 Liu, P., Song, M., Zhao, T., Gunthe, S. S., Ham, S., He, Y., Qin, Y. M., Gong, Z.,

635 Amorim, J. C., Bertram, A. K., and Martin, S. T.: Resolving the mechanisms of

636 hygroscopic growth and cloud condensation nuclei activity for organic particulate

637 matter, Nat. Commun., 9, 4076, 2018.

638   Ma, Q., He, H., Liu, Y.: In situ DRIFTS study of hygroscopic behavior of mineral

639   aerosol, J. Environ. Sci., 22(4), 555–560, 2010.

640   Matthews, H. D., Gillett, N. P., Stott, P. A., and Zickfeld, K.: The proportionality of

641   global warming to cumulative carbon emissions, Nature, 459, 829–832, 2009.

642   Nakamura, M., Ohba, T., Branton, P., Kanoh, H., and Kaneko, K.: Equilibrium-time

643   and pore width dependent hysteresis of water adsorption isotherm on hydrophobic

644   microporous carbons, Carbon, 48, 2549–2553, 2010.

645   Nguyen, T. X., and Bhatia, S. K.: How water adsorbs in hydrophobic nanospaces, J.

646   Phys. Chem. C, 115, 16606–16612, 2011.

647   Nienow, A. M., Roberts, J. T.: Heterogeneous chemistry of carbon aerosols, Rev. Phys.

648   Chem., 57, 105–128, 2006.

649   Ohba, T., and Kaneko, K.: Kinetically forbidden transformations of water molecular

650   assemblies in hydrophobic micropores, Langmuir, 27, 7609–7613, 2011.

651   Petters, S. S., Pagonis, D., Claflin, M. S., Levin, E. J. T., Petters, M. D., Ziemann, P. J.,

652   and Kreidenweis, S. M.: Hygroscopicity of organic compounds as a function of

653   carbon chain length and carboxyl, hydroperoxy, and carbonyl functional groups, J.

654   Phys. Chem. A.J. Phys. Chem. A., 121 (27), 5164–5174, 2017.

655   Pimenta, M. A., Dresselhaus, G., Dresselhaus, M. S., Cancado, L. G., Jorio, A., and

656   Saito, R.: Studying disorder in graphite-based systems by Raman spectroscopy,

657   Phys. Chem. Chem. Phys., 9, 1276–1291, 2007.

658   Posfai, M., Simonics, R., Li, J., Hobbs, P. V., and Buseck, P. R.: Individual aerosol

659   particles from biomass burning from southern Africa: 1. Compositions and size

660   distributions of carbonaceous particles, J. Geophys. Res., 108, 8483, 2003.

661   Powelson, M. H., Espelien, B. M., Hawkins, L. N., Galloway, M. M., and De Haan, D.

662   O.: Brown carbon formation by aqueous-phase carbonyl compound reactions with

663   amines and ammonium sulfate, Environ. Sci. Technol., 48, 985–993, 2014.

664   Preturlan, J. G. D., Vieille, L., Quiligotti, S., and Favergeon, L.: Comprehensive

665   thermodynamic study of the calcium sulfate–water vapor system. Part 1:

666   experimental measurements and phase equilibria, Ind. Eng. Chem. Res., 58, 22,

667   9596–9606, 2019.

668   Qiu, C., Khalizov, A. F., and Zhang, R.: Soot aging from OH-Initiated oxidation of

669   toluene, Environ. Sci. Technol., 46, 9464−9472, 2012.

670   Reid, J. S., Koppmann, R., Eck, T. F., and Eleuterio, D. P.: A review of biomass

671   burning emissions part II: intensive physical properties of biomass burning particles,

672   Atmos. Chem. Phys., 5, 799–825, 2005.

673   Ribeiro, A. M., Sauer, T. P., Grande, C. A., Moreira, R. F. P. M., Loureiro, J. M., and

674   Rodrigues, A. E.: Adsorption equilibrium and kinetics of water vapor on different

675   adsorbents, Ind. Eng. Chem. Res., 47, 18, 7019–7026, 2008.

676   Rosas, J. M., Bedia, J., Miraso, J. R., and Cordero, T.: Preparation of hemp-derived

677   activated carbon monoliths, adsorption of water vapor, Ind. Eng. Chem. Res., 47, 4,

678   1288–1296, 2008.

679   Schwarz, J. P., Spackman, J. R., Fahey, D. W., Gao, R. S., Lohmann, U., Stier, P.,

680   Watts, L. A., Thomson, D. S., Lack, D. A., Pfister, L., Mahoney, M. J.,

681   Baumgardner, D., Wilson, J. C., and Reeves, J. M.: Coatings and their enhancement

682   of black carbon light absorption in the tropical atmosphere, J. Geophys. Res., 113,

683   D03203, 2008.

684   Seisel, S., Pashkova, A., Lian, Y., and Zellner, R.: Water uptake on mineral dust and

685   soot: a fundamental view of the hydrophilicity of atmospheric particles, Faraday

686   Discuss., 130, 437–451, 2005.

687   Sjogren, S., Gysel, M., Weingartner, E., Baltensperger, U., Cubison, M. J., Coe, H.,

688 Zardini, A. A., Marcolli, C., Krieger, U. K., and Peter, T.: Hygroscopic growth and

689   water uptake kinetics of two-phase aerosol particles consisting of ammonium

690   sulfate, adipic and humic acid mixtures, Aerosol Science, 38, 157–171, 2007.

691 Song, J., Peng, P., and Huang, W.: Black carbon and kerogen in soils and sediments. 1.

692   Quantification and characterization, Environ, Sci. Technol., 36, 3960–3967, 2002.

693 Song, W., and Boily, J. F.: Water vapor adsorption on goethite, Environ. Sci. Technol.,

694   47, 7171–7177, 2013.

695 Stanislav, V., Vassilev, D. B., Andersen, L. K., and Vassileva, C. G.: An overview of

696   the composition and application of biomass ash. Part 1. Phase-mineral and chemical

697   composition and classification, Fuel, 105, 40–76, 2013.

698 Stemmler, K., Vlasenko, A., Guimbaud, C., and Ammann, M.: The effect of fatty acid

699   surfactants on the uptake of nitric acid to deliquesced NaCl aerosol, Atmos. Chem.

700   Phys., 2008, 8 (17), 5127–5141, 2008.

701 Suda, S. R., Petters, M. D., Yeh, G. K. Strollo, C., Matsunaga, A., Faulhaber, A.,

702   Ziemann, P. J., Prenni, A. J., Carrico, C. M., Sullivan, R. C., and Kreidenweis, S.

703   M.: Influence of functional groups on organic aerosol cloud condensation nucleus

704   activity, Environ. Sci. Technol., 48, 10182–10190, 2014.

705 Velasco, L. F., Remy Guillet, N. R., Dobos, G., Thommes, M., and Lodewyckx, P.:

706   Towards a better understanding of water adsorption hysteresis in activated carbons

707   by scanning isotherms, Carbon, 96, 753–758, 2016.

708 Wei, S., Zhu, M., Fan, X., Song, J., Peng, P., Li, K., Jia, W., and Song, H.: Influence

709   of pyrolysis temperature and feedstock on carbon fractions of biochar produced

710   from pyrolysis of rice straw, pine wood, pig manure and sewage sludge,

711   Chemosphere, 218, 624–631, 2019.

712 Xiao, J., Liu, Z., Kim, K., Chen, Y., Yan, J., Li, Z., and Wang, W.: S/O-Functionalities

713   on modified carbon materials governing adsorption of water vapor, J. Phys. Chem.

714   C., 117, 23057−23065, 2013.

715   Xiao, X., Chen, B., Chen, Z., Zhu, L., and Schnoor, J. L.: Insight into multiple and

716   multilevel structures of biochars and their potential environmental applications: A

717   critical review, Environ. Sci. Technol., 52(9), 5027−5047, 2018.

718   Yuan, J. F., Huang, X. F., Cao, L. M., Cui, J., Zhu, Q., Huang, C. N., Lan, Z. J., and

719   He, L.Y.: Light absorption of brown carbon aerosol in the PRD region of China,

720   Atmos. Chem. Phys. Discuss., 15, 28453–28482, 2015.

721   Yuan, W., Li, X., Pan, Z., Connell, L. D., Li, S., and He, J.: Experimental

722   investigation of interactions between water and a lower silurian chinese shale,

723   Energy Fuels, 28, 4925−4933, 2014.

724   Zhang, R., Khalizov, A., Wang, L., Hu. M., and Xu, W.: Nucleation and growth of

725   nanoparticles in the atmosphere, Chem. Rev., 112, 3, 1957–2011, 2012.

726   Zuend, A., Marcolli, C., Booth, A. M., Lienhard, D. M., Soonsin, V., Krieger, U. K.,

727   Topping, D. O., McFiggans, G., Peter, T., and Seinfeld, J. H.: New and extended

728   parameterization of the thermodynamic model AIOMFAC: Calculation of activity

729   coefficients for organic-inorganic mixtures containing carboxyl, hydroxyl, carbonyl,

730   ether, ester, alkenyl, alkyl, and aromatic functional groups, Atmos. Chem. Phys., 11,

731   9155–9206, 2011.